RSC Advances

PAPER

View Article Online
View Journal | View Issue

Cite this: *RSC Adv.*, 2023, **13**, 10861

Experimental and theoretical study of catalytic dye degradation and bactericidal potential of multiple phase Bi and MoS_2 doped SnO_2 quantum dots†

Ayesha Habib,[a] Muhammad Ikram, *[a] Ali Haider, [b] Anwar Ul-Hamid, [c] Iram Shahzadi,[d] Junaid Haider,[e] Mohammed Benali Kanoun,[f] Souraya Goumri-Said [g] and Walid Nabgan *[h]

In the present study, different concentrations (1 and 3%) of Bi were incorporated into a fixed amount of molybdenum disulfide (MoS_2) and SnO_2 quantum dots (QDs) by co-precipitation technique. This research aimed to increase the efficacy of dye degradation and bactericidal behavior of SnO_2. The high recombination rate of SnO_2 can be decreased upon doping with two-dimensional materials (MoS_2 nanosheets) and Bi metal. These binary dopants-based SnO_2 showed a significant role in methylene blue (MB) dye degradation in various pH media and antimicrobial potential as more active sites are provided by nanostructured MoS_2 and Bi^{3+} is responsible for producing a variety of different oxygen vacancies within SnO_2. The prepared QDs were described *via* morphology, optical characteristics, elemental composition, functional group, phase formation, crystallinity, and *d*-spacing. In contrast, antimicrobial activity was checked at high and low dosages against *Escherichia coli* (*E. coli*) and the inhibition zone was calculated utilizing a Vernier caliper. Furthermore, prepared samples have expressed substantial antimicrobial effects against *E. coli*. To further explore the interactions between the MB and Bi/MoS_2–SnO_2 composite, we modeled and calculated the MB adsorption using density functional theory and the Heyd–Scuseria–Ernzerhof hybrid (HSE06) approach. There is a relatively strong interaction between the MB molecule and Bi/MoS_2–SnO_2 composite.

Received 1st February 2023
Accepted 30th March 2023

DOI: 10.1039/d3ra00698k

rsc.li/rsc-advances

1 Introduction

The most fundamental requirement for all living things is clean water.[1] An essential component of life is organic compounds but they also have a significant function in the degradation of the natural environment and have essential practical benefits in businesses such as the cosmetics, painting, and dying industries. Dyes are organic compounds, categorized into two types, cationic and anionic. Heavy metal ions (lead, chromium, arsenic), azo dyes such as methylene blue (MB) and rhodamine B (RhB), and phenol present in wastewater find their way to the aqueous environment and pollute the water. This results in harm to all marine life, land animals, and plant life[2–7] and has adverse effects on human health, such as anemia, bladder irritation, gastrointestinal issues, and so on. Furthermore, waterborne microbes namely Gram-positive *Staphylococcus aureus* (*S. aureus*) and Gram-negative *Escherichia coli* (*E. coli*) make a route of nosocomial disease in human beings.[8]

Catalysis is a significant process that focuses on nano-material semiconductors owing to chemical stability, their low toxicity, and environmental friendliness.[9] The admiration of semiconductor nanoparticles has increased attributed to catalysis capabilities and photo reactivity. Numerous transition-metal oxides, ZnO, SnO_2, Fe_2O_3, TiO_2, and Bi_2O_3 have been employed in photocatalysis to convert multiple organic contaminants into harmless CO_2 and H_2O. Among them, SnO_2 has now been suggested as a potentially useful photocatalyst due to its low toxicity, efficiency, relatively high chemical stability and cost-effective.[10]

Additionally, SnO_2 is an n-type semiconductor that has a wide band gap energy (E_g) of 3.6 eV, less resistivity, high electron mobility (200 $cm^2\ V^{-1}\ s^{-1}$), and photoexcited e^-/h^+ by

[a]*Solar Cell Applications Research Lab, Department of Physics, Government College University Lahore, Lahore, 54000, Punjab, Pakistan. E-mail: dr.muhammadikram@gcu.edu.pk*

[b]*Department of Clinical Sciences, Faculty of Veterinary and Animal Sciences, Muhammad Nawaz Shareef University of Agriculture (MNSUA) Multan, 66000, Pakistan*

[c]*Core Research Facilities, Research Institute, King Fahd University of Petroleum & Minerals, Dhahran, 31261, Saudi Arabia*

[d]*Faculty of Pharmacy, The University of Lahore, 54000, Pakistan*

[e]*Tianjin Institute of Industrial Biotechnology, Chinese Academy of Sciences, Tianjin 300308, China*

[f]*Department of Mathematics and Sciences, College of Humanities and Sciences, Prince Sultan University, P.O. Box 66833, Riyadh 11586, Saudi Arabia*

[g]*Physics Department, College of Science and General Studies, Alfaisal University, P.O. Box 50927, Riyadh 11533, Saudi Arabia*

[h]*Departament d'Enginyeria Química, Universitat Rovira i Virgili, Av Països Catalans 26, 43007, Tarragona, Spain. E-mail: wnabgan@gmail.com; walid.nabgan@urv.cat*

† Electronic supplementary information (ESI) available. See DOI: https://doi.org/10.1039/d3ra00698k

reason of these characteristics, it is suitable for various applications.[11–17] The quick e^-/h^+ recombination of SnO_2 limits its applications to reduce dye effluents.[18,19] Abdel-Messih *et al.* SnO_2 prepared through sol–gel methodology, exhibited 10% decolorization of RhB within 120 min under UV-light. Sayfa Bano *et al.* Synthesized SnO_2 *via* chemical oxidation polymerization, co-precipitation method, and RhB removal using UV light to achieve 10% methanol efficacy within 20 min.[20,21] To deal with the aforesaid flaw, several approaches such as oxygen vacancy formation and doping with non-metals, carbon materials, and metals heterostructure development were applied for narrowing the E_g and expanding the absorption spectral response towards visible area.[22] Vadivel and Rajarajan[23] and Rawal *et al.*[24] demonstrated that tungsten (W) doping improved the dye degradation capabilities of SnO_2 against different dye contaminants. Sharf Illahi Siddiqui *et al.* Prepared monohybrids Fe_2O_3/SnO_2 and showed 95% degradation of MB.[25]

Metal dichalcogenides have recently been discovered to be remarkable in the realm of dye degradation,[22] in this work fixed concentration of MoS_2 doped into SnO_2. MoS_2 acts as one of the valuable materials for catalysis. It demonstrates the particular optical features, chemical inertness, and high conductivity that show it as cardinal for numerous applications (phototransistors, sensing, catalysis).[26,27] Nanostructured MoS_2 gives more active sites other than bulk MoS_2 due to the reason it has a direct band gap.[28,29] Non-metal based doping has significant promise for biosensing, contaminants removal, and bioimaging purposes,[30] herein bismuth has been chosen as a doping agent. Two different (dichalcogenides and post-transition) metals doped into SnO_2 and a relative discussion of their applications as well as characteristics, which to the extent feasible knowledge has not yet been published. Distinctive modification of SnO_2 has been an expected promising approach to get better efficacy of CA at small time intervals and microbial activity.

In the current work, the co-precipitation technique was used to introduce MoS_2 and Bi into SnO_2 to synthesize Bi-doped MoS_2–SnO_2 QDs. The prepared QDs investigated the antibacterial potential for the inhibition of *E. coli* and improved degradation of MB. Additionally, detailed analyses of synthesized QDs were examined by numerous techniques.

2 Experimental section

2.1 Material

Tin chloride dihydrated ($SnCl_2 \cdot H_2O$, 98%), bulk molybdenum disulfide (~6 μm, 99%), sodium hydroxide (NaOH, 98%), was acquired from Sigma-Aldrich (Germany). Bismuth nitrate ($Bi(NO_3)_3 \cdot 5H_2O$) was obtained from England. HCl (37% dilute) and sodium nitrate ($NaNO_3$) were received from 'Analar' and 'Merck', respectively. All materials had been consumed exactly as received.

2.2 Liquid-phase exfoliation of MoS_2

The technique applied to prepare liquid phase exfoliated (LPE) MoS_2 nanosheets (NSs) is depicted in Fig. 1a. Using a beaker, $NaNO_3$ (6.0 g) was dissolved in 16.0 mL of 37% diluted HCl. After that, bulk MoS_2 (1.2 g) was incorporated, and the reaction was stopped by the addition of an appropriate quantity of H_2O. The suspension was then ultrasonically exfoliated for 5 h at 30 °C in a setup designed to capture hazardous gas. Finally, to extract the nanosheet, the resulting supernatant fraction was centrifuged for 30 min at 6000 rpm. Precipitated formed grayish black MoS_2 nanosheets were obtained.[31]

2.3 Synthesis of Bi-doped MoS_2–SnO_2

The chemical co-precipitation approach was utilized for the preparation of bare SnO_2 and Bi/MoS_2-doped SnO_2 (Fig. 1b). A solution of $SnCl_2$ with a concentration of 0.5 M was prepared and subjected to heating at 80 °C while constant stirring was maintained. Hereafter, a fixed amount (11.28 mg) of MoS_2 had been integrated into the SnO_2 solution. After that various concentrations (5.64 and 16.92 mg) of Bi were incorporated into the solution mixture at continuous stirring. After half an h, 1 M NaOH was incorporated into the aforesaid colloidal solution in a drop-by-drop manner to sustain the pH ~ 10. After that, the produced precipitates have been washed many times by centrifugation at 7000 rpm for 7 min to achieve a product that was free from contaminants, and therefore they were dried at 90 °C for 12 h. The final product was crushed into fine powder.

2.4 Catalysis

In the presence of $NaBH_4$, the catalytic activity of SnO_2 and Bi/MoS_2-doped SnO_2 QDs was evaluated by the decolorization of MB into leucomethylene blue (LMB). Positively charged MB dye is utilized as an oxidizing agent, colorless when reduced and blue color when oxidized[32] and $NaBH_4$ is act as a reducing agent. MB (3 mL) was incorporated in 0.1 M $NaBH_4$ solution (400 μL) in a quartz cell. Moreover, the solution of MB was dissolved in 400 μL prepared QDs. The absorption reaction process had been examined spectrophotometrically at regular intervals. The percentage of dye degradation was determined as:

$$\%\ \text{degradation} = \frac{C_0 - C_t}{C_0} \times 100$$

where C_0 and C_t are referred to as the initial and final MB concentrations, respectively.

2.5 Isolation and identification of MDR *E. coli*

2.5.1 Sample collection. From determined breastfeeding cows sold at several markets, farms, and veterinary clinics in Punjab Pakistan, raw milk samples were obtained by direct milking to decontaminating glassware. After being collected at 4 °C, raw milk was promptly deposited in the laboratory. Coliforms count in raw milk was carried out on MacConkey agar. All plates were incubated at 37 °C for 48 h.

2.5.2 Identification and characterization of bacterial isolates. The initial identification of *E. coli* was based on a variety of biochemical tests and Gram stain colonial morphology, under Bergey's Manual of Determinative Bacteriology.[33]

2.5.3 Antibiotic susceptibility. The disk diffusion method of Bauer' *et al.*[34] Mueller Hinton agar (MHA) was used for the

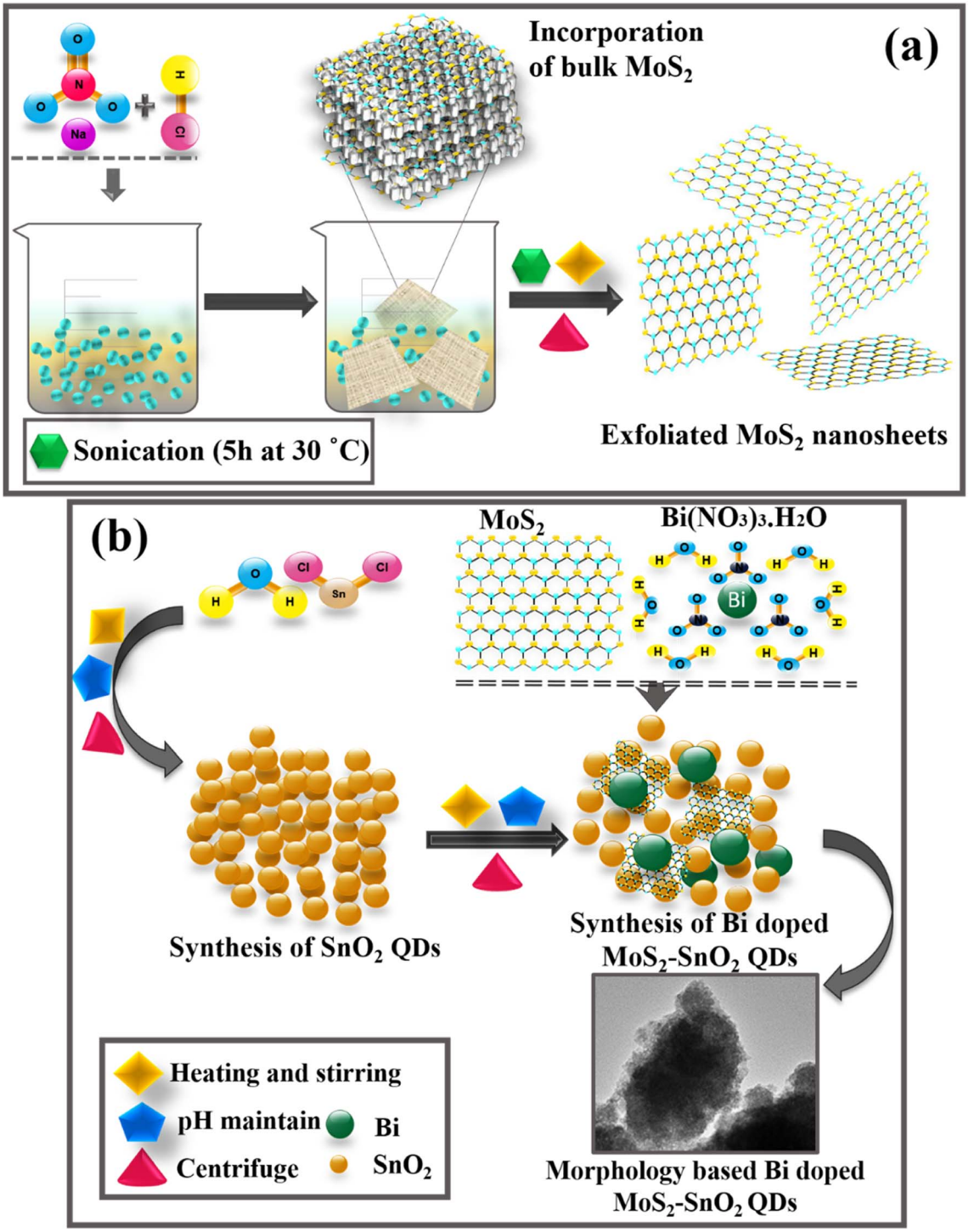

Fig. 1 (a) Schematic diagram of MoS_2 and, (b) synthesis of Bi/MoS_2-doped SnO_2.

antibiotic susceptibility test. This test was performed to demonstrate the resistance of *E. coli* to various kinds of antibiotics; imipenem (Imi) 10 μg (carbapenem), ciprofloxacin (Cip) 5 μg (quinolones), azithromycin (Azm) 15 μg (macrolides), tetracycline (Te) 30 μg (tetracyclines), ceftriaxone (Cro) 30 μg (cephalosporins), amoxycillin (A) 30 μg (penicillins) and gentamicin (Gm) 10 μg (aminoglycosides).[35] Uncontaminating cultures of *E. coli* were grown and engaged to 0.5 MacFarland turbidity. On Muller Hinton Agar (MHA) (Oxoid Limited, Basingstoke, UK), it was then expanded plate and the prevention of overlapping of inhibition zones. The antibiotic discs were spaced apart on the surface of the inoculated plate. Plates were incubated for 24 h at 37 °C and according to the clinical and laboratory standard institute, the consequences were

elucidated.[36] A bacterium having at least three antibiotic resistances was announced as MRD.[37]

2.5.4 Antimicrobial activity. The *in vitro* antibacterial action potential of NSs on 10 representative isolates of MRD *E. coli* assembled from mastitis milk was estimated using an agar well diffusion approach. On MacConkey agar, Petri dishes were swabbed with 1.5×10^8 CFU mL^{-1} (0.5 MacFarland standard) MRD *E. coli*. An Uninfected cork borer was utilized to form wells of 6 mm in diameter. Various concentrations of Bi/MoS_2 doped SnO_2 were applied as (0.5 mg/50 μL) and (1.0 mg/50 μL). DI water was utilized as the negative control (50 μL) and ciprofloxacin (0.005 mg/50 μL) as the positive control.[38]

2.5.5 Statistical analysis. The antibacterial effectiveness had been estimated in respect of inhibition zone size (mm), and inhibition zone diameters were statistically investigated using one-way analysis of variance (ANOVA) in SPSS 20.[39]

2.5.6 Characterizations. The crystallographic behavior of SnO_2 and Bi/MoS_2-doped SnO_2 QDs were evaluated using a PANalytical Xpert PRO X-ray diffraction (XRD) instrument in the 20–70° range of 2θ using Cu Kα radiation ($\lambda \sim 0.154$ nm). A PerkinElmer 3100 FTIR spectrometer was used with 32 scans in the 4000–400 cm^{-1} range to detect the presence of functional groups in the synthesized catalyst. A UV-Vis Genesys 10S spectrophotometer with a wavelength range of 210–600 nm was employed to analyze the optical properties. The morphological characteristics of QDs were studied using the JSM-6460LV FE-SEM scheme in combined with an EDS spectrometer.

3 Results and discussion

MoS_2 nanosheets were synthesized by liquid-phase exfoliation, illustrated in Fig. 1a. Bi-doped MoS_2–SnO_2 QDs were synthesized using a cost-effective co-precipitation method with different concentrations (1 and 3%) of Bi and fix concentration of MoS_2 dopant as shown in schematic diagram Fig. 1b.

XRD analysis has been utilized to examine the crystallographic structure, and phase purity of a material, 2θ ranging from 20° to 70° of SnO_2 and Bi (1 and 3%) MoS_2-doped SnO_2 (Fig. 2a). Diffracted peaks emerged at 26.26° (110), 33.87° (101), 37.86° (200), 51.40° (211), 54.79° (220), 61.76° (310) and 65.75°

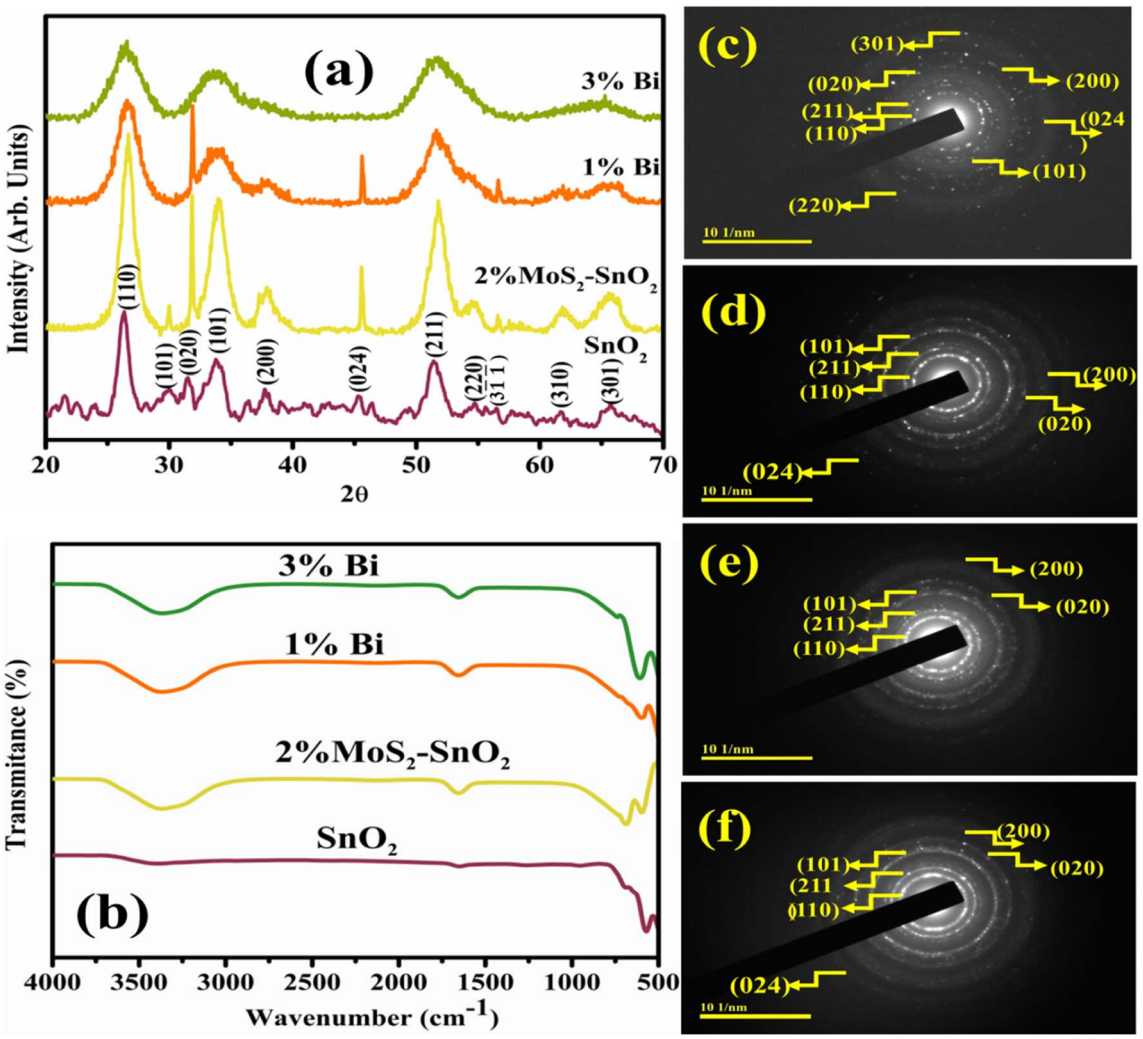

Fig. 2 (a) XRD patterns, (b) FTIR spectra, and (c–f) SAED images of SnO_2, MoS_2-doped SnO_2, and Bi (1 and 3%)/MoS_2-doped SnO_2 QDs.

(301) revealed the tetragonal phase (t-SnO_2) authenticated by (JCPDF 01-077-0452/00-046-1088) and 31.48° (020) to the orthorhombic phase (o-SnO_2). Furthermore, peaks at 29.88° (101) 45.32° (024), and 56.49° (3-1-1) owing to SnO and Sn_2O_3 respectively confirmed by (JCPDF 00-006-0395/01-077-2296/00-025-1259). Different phases of tin oxide were observed. The peak intensity of MoS_2-doped SnO_2 was sharp and less broadened, advocating the crystallinity is enhanced and crystal size increased.[40] Upon doping of different concentrations of Bi, the peak intensity decreased and broadened as compared to the pure sample. Suppression in intensity ascribed to Bi has an inhibitory impact on crystallinity and the larger ionic radii of Bi corresponding to Sn and O, which minimize the ability of its substitution in SnO_2.[41] Upon incorporation of Bi, few peaks were diminished, suggesting that Bi has an inhibitory effect on crystallinity and particle growth because Bi ions at the particle's surface compete for rearrangement and diffusion in SnO_2; hence crystal growth vanished.[42] The crystallite size calculated using the Debye–Scherrer formula from the most intense peak of prepared samples was 9.21 nm, 9.59 nm, 3.74 nm, and 3.94 nm for SnO_2, MoS_2-doped SnO_2 and, Bi (1 and 3 wt%)/MoS_2-doped SnO_2 QDs, respectively.

FTIR analysis was investigated to determine the presence of the functional group, modes of vibration for chemical bonds, and surface chemistry of synthesized samples in the 4000–400 cm^{-1} wavenumber range (Fig. 2b). The bending vibration of water and stretching vibration of absorbed hydroxyl function group were associated with the band appeared at 1640 cm^{-1} and 3300–3500 cm^{-1} respectively.[43,44] The transmission band at 581 cm^{-1} was manifested to O–Sn–O bending and stretching modes of SnO_2 (ref. 45) and a possible O–Sn–O mode of vibration has been assigned to the band at 682 cm^{-1}.[46] No extra peaks were generated after doping which might be due to the incorporation of less concentration of dopants.

Bright dots in SAED pattern (Fig. 2c–f) depict the crystalline nature of the as-synthesized specimen. The indexing of SAED patterns revealed the rings were found to correlate to the planes (110), (211), (101), (020), (200), (024), (301), and (220). The planes and the observed peaks are well agreed with XRD and substantiate one another result.

The optical properties were estimated by electronic spectroscopy in the range of 200 to 800 nm. In UV-vis spectra, the 3-D quantum confinement effect was observed by semiconductor NSs. The absorption peak at 285 nm for synthesized SnO_2 was revealed by electronic spectra (Fig. 3a). Similarly, the absorption peaks of MoS_2-doped SnO_2, and Bi (1 and 3 wt%)/MoS_2-doped SnO_2 were observed to be increased and the transfer of electrons was π–π^*.[47] Hence, the absorption ability of light increased with MoS_2 and the concentration of Bi. Absorption spectra shifted towards a longer wavelength and the absorption edge indicated the redshift.[48–50] Tauc plot was used to measure the band gap energy (E_g) of bare and doped QDs. SnO_2 QDs have direct $E_g \sim$ 4.30 eV while E_g of doped samples was decreased as concentration increased (4.20–3.59 eV), mentioned in Fig. 3b.

Various proportions of elements (Sn, O, Mo, S, Bi, Na, Cl) of Bi (1 and 3%)/MoS_2-doped SnO_2 QDs represented by EDS, elaborated in Fig. S1a–d.† Elemental constituents of as-prepared samples using specific colors described by mapping (Fig. S1e†). A pure sample is authenticated by the strong peaks of O and Sn whereas the peaks of Mo, S, and Bi represented the existence of MoS_2 and Bi in SnO_2. Furthermore, sodium (Na) peak was observed by NaOH used to maintain the pH of samples, and the chlorine (Cl) peak behave as an impurity attributed to the precursor used for synthesis. The holder and coating used for the EDS analysis resulted in a minor trace of Au peak. Electrostatic charging affected the samples throughout the SEM examination, to reduce charging damage, Au was used for SEM/EDS analysis.[51]

TEM was utilized to identify the morphology and structure of as synthesized Bi/MoS_2-doped SnO_2 as shown in Fig. 4a–d. In Fig. 4a, TEM image represents the morphology of QDs of the control sample SnO_2. Upon doping of MoS_2 into QDs (Fig. 4b), seems that nanosheets overlapped the SnO_2 quantum dots. In Fig. 4c, the addition of Bi (1%) into the binary system (MoS_2–SnO_2) revealed the agglomeration of QDs which can be attributed to hydrogen bonding as the solvent was DI water. A high

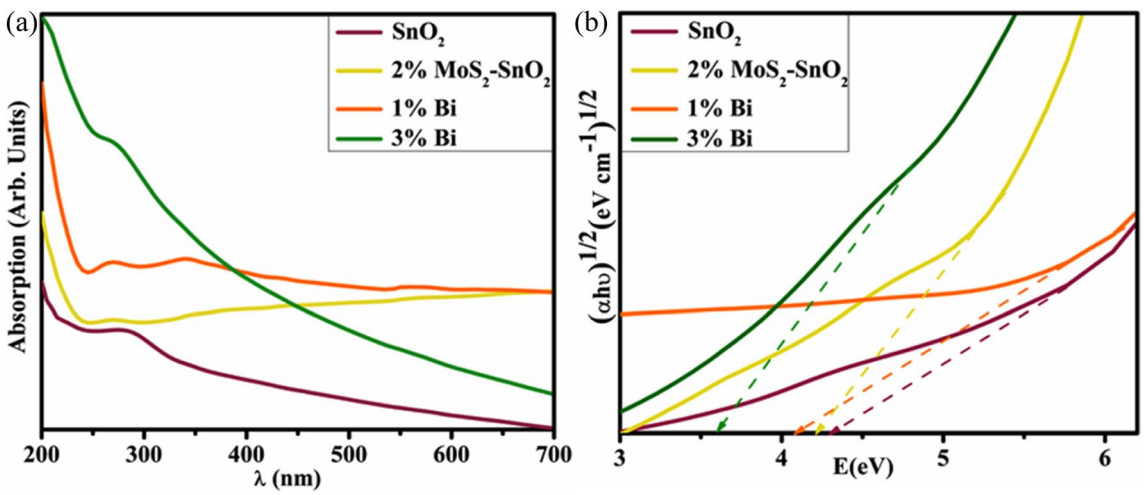

Fig. 3 (a) Absorbance spectra and, (b) calculated band gap energy of SnO_2, MoS_2-doped SnO_2, and Bi (1 and 3%)/MoS_2-doped SnO_2 QDs.

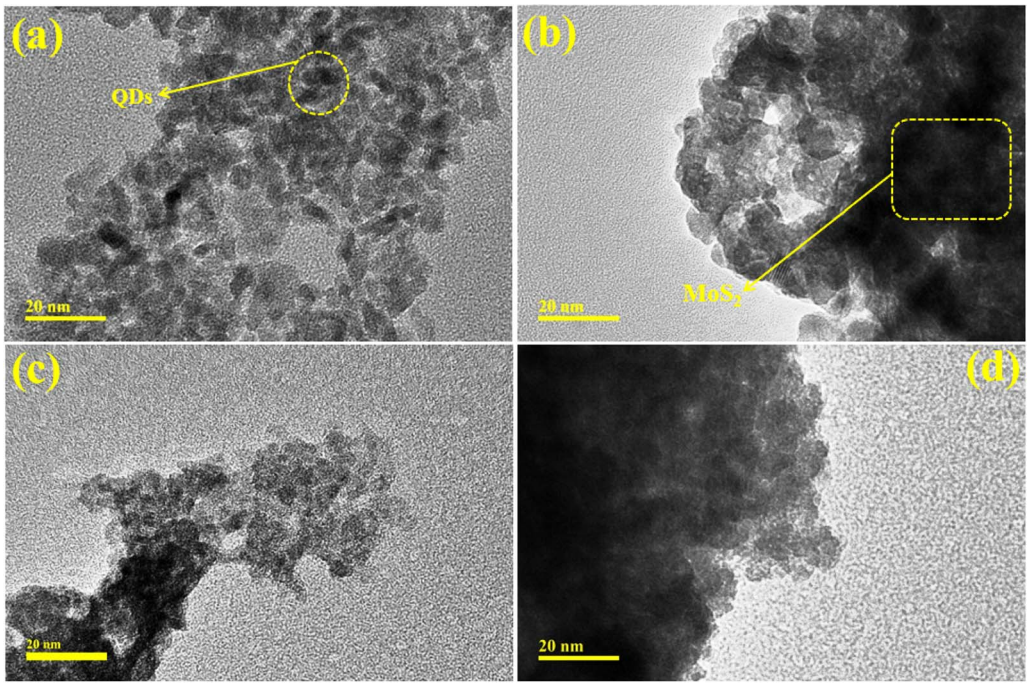

Fig. 4 TEM images of (a) SnO_2 (b) MoS_2-doped SnO_2 and (c and d) Bi (1 and 3%)/MoS_2-doped SnO_2 QDs.

degree of agglomeration was observed upon a higher concentration of Bi (3%) into MoS_2–SnO_2 (Fig. 4d). The average particle size of SnO_2 QDs (Fig. 4a) ranging from 4.55 to 7.95 nm was calculated using Image J. software.

Interlayer *d*-spacing was calculated for all prepared QDs using high-resolution (10 nm) TEM images, as proclaimed in Fig. S2a–d.† The interlayer *d*-spacing of SnO_2 QDs was 0.23 nm (200). The *d*-spacing of doped samples were 0.23, 0.20, 0.19, and 0.17 nm along with the planes (112), (024), and (211) respectively, matched well with XRD result. The interlayer *d*-spacing was decreased because of the overlapping of MoS_2 on QDs which was well consistent with TEM analysis.

MB was used as an alternative contaminant to evaluate the catalytic application of synthesized samples. CA measurements were used to determine the degradation rate of synthetic dyes in the presence of $NaBH_4$ and the synthesized nanocatalyst (Fig. S3†). The general mechanism has an electron donor $NaBH_4$ which donates an electron to the proceeding chemical reaction to behave as a reductant while MB accepts an electron from the reducing agent to serve as an oxidant and oxidation–reduction reaction exhibits. Initially, $NaBH_4$ and dye adsorb on the surface of the catalyst and give root to the breakage of MB to LMB. Breakage of double bonds from aromatic rings and dye's N happens when MB accepts the electron and H atom from BH_4^-. H atom attaches to double bonded N atom of dye molecules *via* double bond breakage while e^- is accepted by the positively charged N atom, as a result, π conjugation takes place. Although the reaction is favorable in thermodynamics in the absence of a catalyst but not valuable in kinetics. MB degradation was prolonged and time taking in the presence of $NaBH_4$. To overwhelm these difficulties, the nanocatalyst was dissolved in a redox reaction providing a path to electrons and permits to migrate from BH^-_4 to MB. QDs increased the adsorption rate of dye and BH_4^- ions and several active sites enhanced their reactivity which increase the efficiency of dye degradation.[52–55] The catalytic activity was affected by the particle size as a surface-to-volume ratio is high in small-sized particles, consequently, degradation increased.[32]

Electronic spectroscopy was used to observe the catalytic activity of pure and doped SnO_2 QDs for MB degradation. As mentioned in Fig. 5a–c, SnO_2, MoS_2-doped SnO_2, and Bi (1 and 3%)/MoS_2-doped SnO_2 QDs manifested the maximal degradation of 78.74, 99.9, 99.9, and 99.9% in acidic, 79.70, 89.85, 94.92 and 99.9% in basic, and 58.79, 63.36, 63.36 and 67.94%, in neutral medium respectively. The factors that affected the CA were crystallite size, medium pH, and surface area. The maximum degradation in MB was investigated in Bi (1%)/MoS_2-doped SnO_2 in acidic, basic, and neutral media. In an acidic medium, both dopants MoS_2 and Bi showed maximum degradation attributable to the utmost fabrication of H ions adsorbed on the QDs.[56] In a basic medium, the surface of the catalyst gravitates to gain a negative charge while the positively charged surfaces of the catalyst constrain the absorption of cationic adsorbate species in acidic environment.[57,58] MoS_2 enhanced the catalytic activity as it helped to transfer electrons (electron capture) as compared to the control sample.[59] The defects as well as disorders ascribed to the Bi^{3+}, act as the trapping center for e^-/h^+ pairs, and effectively hinder the photo-generated charge carriers recombination.[60]

Antibacterial activity of undoped and MoS_2-doped SnO_2 and Bi (1 and 3%)/MoS_2-doped SnO_2 QDs is encapsulated in the Table 1. At low and high dosages, inhibition diameters were

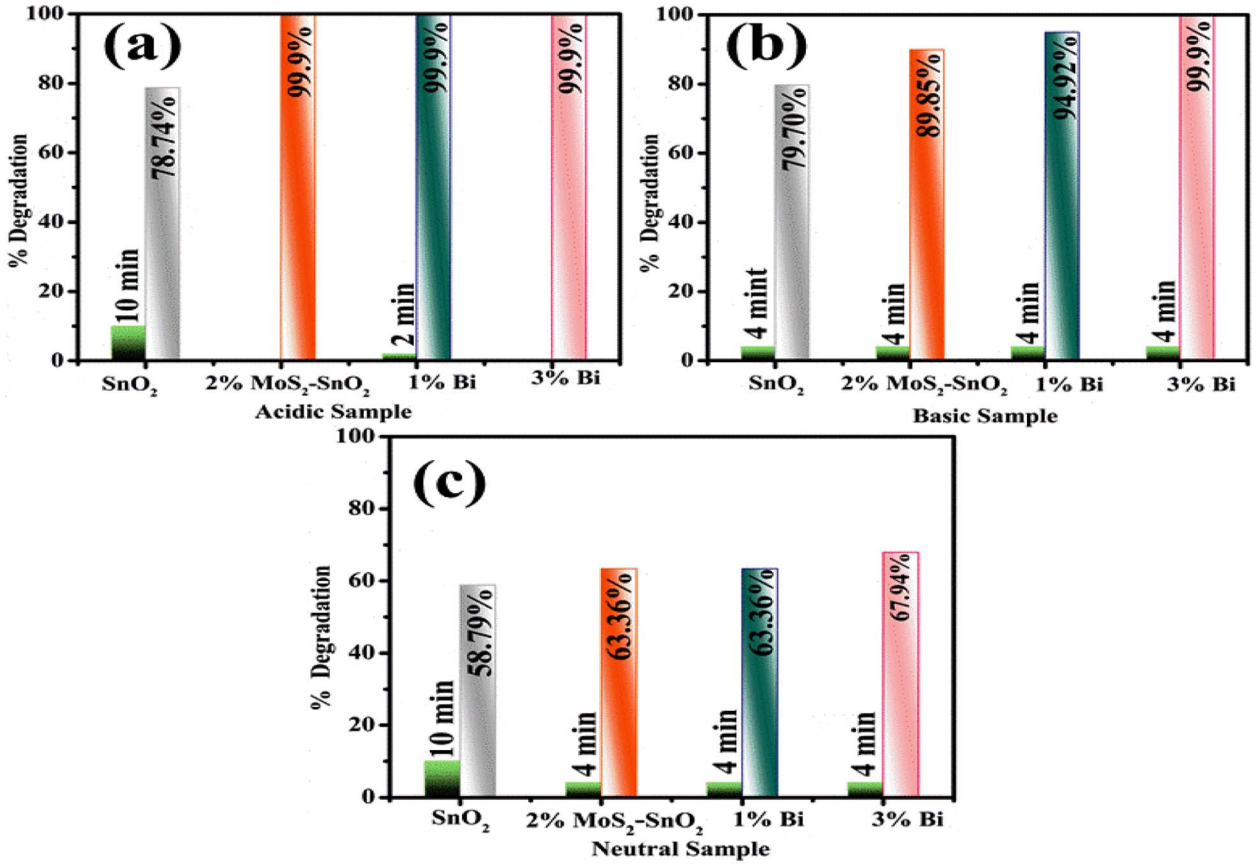

Fig. 5 Catalysis of SnO_2, MoS_2-doped SnO_2 and Bi (1 and 3%)/MoS_2-doped SnO_2 QDs in (a) acidic, (b) basic, and (c) neutral media.

reported in *E. coli* from (0.34–2.90) to (1.75–3.15) respectively, and displayed in Table 1. Additionally, the inhibition zone for ciprofloxacin (positive control) was estimated to be 4.85 mm corresponding to zero mm DI water (negative control) against *E. coli*. Pristine QDs illustrated less activity against *E. coli* rather than Bi/MoS_2-doped SnO_2. Upon incorporation of MoS_2, antibacterial activity enhanced because MoS_2 is useful for increasing surface area and reducing particle size. The cell wall of bacteria is easily penetrated by small size particles.[61] The incorporation of Bi prevents the formation of biofilm and disrupts bacterial membrane integrity, which could improve Bi delivery inside bacterial cells and, as a result, increase its antimicrobial activity.[62]

Table 1 Antibacterial potential of SnO_2, MoS_2-doped SnO_2 and Bi (1 and 3%)/MoS_2-doped SnO_2 QDs

	Inhibition areas (mm)	
Samples	0.5 mg/50 μL	1.0 mg/50 μL
SnO_2	0.35	1.75
SnO_2–MoS_2	2.40	2.75
1% Bi	2.56	2.95
3% Bi	2.90	3.15
Ciprofloxacin	4.85	4.85
DI water	0	0

The ROS generation (O_2^-, HO_2, OH, and H_2O_2), free radical formation, and reduction in cell membrane integrity have been strongly linked with microbicidal action. The ability of metal oxides to donate electrons generates ROS. The surface of the microbial cell membrane is nanometer-sized porous; hence the sufficient charge and size of nanomaterials pierce the membrane. Cell functions are disrupted by affecting DNA and protein using these nanomaterials and cell performance destroy ultimately.[63] ROS and metal ions released from nanomaterials are intended to generate inhibitory zones (Fig. S4†).

All calculations were performed within the density functional theory using the generalized gradient approximation (GGA) formulated by Perdew–Burke–Ernzerhof[64] for exchange and correlation. We used the computational package QuantumATK,[65] in which employs the linear combination of atomic orbital (LCAO) basis set approach to solve the single particle Kohn–Sham equations. The norm-conserving PseudoDojo pseudopotentials[66] with a medium basis set and a kinetic-energy cutoff energy of 75 Ha were used. For the weak dispersion forces, the DFT-D2 function of Grimme[67] was applied. The Heyd–Scuseria–Ernzerhof hybrid (HSE06) approach was used to obtain the more accurate electronic structures of the materials in the investigation.[68,69] The structure was optimized when the atomic force reached 0.05 eV $Å^{-1}$ and the most significant energy difference between the two stages was less than 10^5 eV. The Brillouin zone is sampled with a $4 \times 4 \times 1$ Monkhorst–Pack

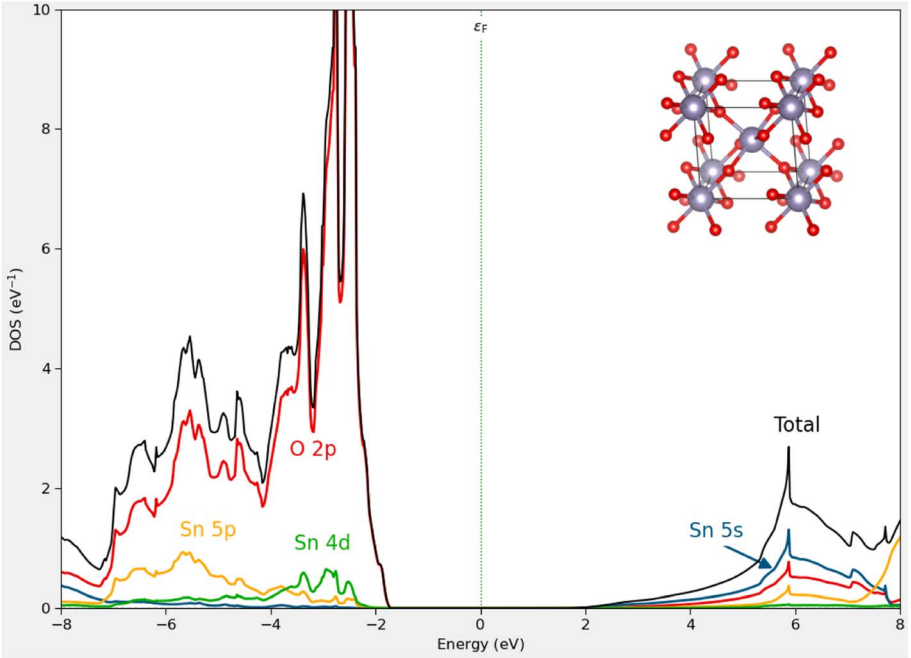

Fig. 6 Calculated total and partial DOS of pristine bulk SnO_2.

grid for the calculations. The optimized lattice parameters of bulk SnO_2 are found to be $a = 4.825$ Å, $c = 3.244$ Å, which matches well with experimental values of $a = 4.737$ Å, $c = 3.186$ Å.[70] We employed a nanocluster derived from stoichiometric cuts from the bulk crystal structure with $(SnO_2)_6$, which retains its atomic structure reasonably well concerning the original bulk atomic ordering and positions after structural relaxation, as shown in Fig. 7. A $3 \times 3 \times 1$ supercell based on a hexagonal unit cell was adopted to model MoS_2 monolayer and a vacuum space of 20 Å was employed in the z-direction to avoid artificial interaction between neighboring layers,[71] as shown in Fig. 7. We calculated the total and partial DOS of bulk SnO_2 using HSE06 functional, as illustrated in Fig. 6. From the analysis of the results, the band gap of bulk SnO_2 is found to be 3.27 eV, which agrees well with the experimental values of 3.60 eV (ref. 72) and other theoretical values.[73] The PDOS demonstrates that the maximum of the valence band is mainly composed of O 2p states and that the minimum of the conduction band is dominated by strongly hybridized Sn 5 s and O 2p states. The calculated HOMO–LUMO gap (5.08 eV) of $(SnO_2)_6$ nanocluster is larger than the band gap for SnO_2 crystal, because of the quantum confinement. The obtained gap value is consistent with our experimental measurements (4.40 eV).

To further explore the interactions between the MB and Bi/MoS_2–SnO_2 composite, we calculated the MB adsorption on the Bi/MoS_2–SnO_2 system. The adsorption energy was calculated using the following expression;[74,75] $E_{ads} = E_{MB+complex} - E_{complex} - E_{MB}$, where $E_{MB+complex}$, $E_{complex}$, and E_{MB} are the total energies of the Bi/MoS_2–SnO_2 composite absorbed MB, the Bi/MoS_2–SnO_2 composite, and the isolated MB molecule, respectively. The calculated E_{ads} with respect to MB on the MoS_2 doped SnO_2 nanocluster and Bi/MoS_2 doped SnO_2 nanocluster are found to be −4.26 eV, and −3.06 eV respectively. Negative adsorption energy corresponds to an exothermic reaction. The MB molecule is found to interact relatively stronger on Bi/MoS_2–SnO_2 composite.

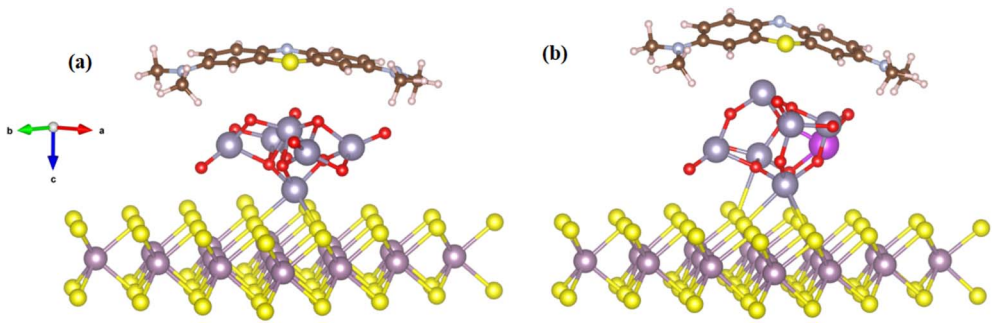

Fig. 7 Optimized adsorption geometries of the MB on (a) MoS_2–SnO_2 system (b) Bi/MoS_2-doped SnO_2 composite (red: O; blue gray: Sn; light purple: Bi; purple: Mo: brown: C; blue: N; yellow: S; gray: H).

4 Conclusion

In this research, Bi/MoS_2-doped SnO_2 QDs have been prepared using a cost-effective co-precipitation method with different concentrations (1 and 3%) of Bi dopant to enhance the dye degradation and antimicrobial activity efficiency. Decreased peak intensity and broadening of FWHM of prepared specimen affirmed by XRD. A significant decrease in E_g was noticed with the higher concentration of dopants. FTIR confirmed the functional groups in prepared QDs while EDS and mapping were used to determine the elemental composition of control and doped samples. QDs morphology was recorded *via* TEM and HR-TEM calculated interplanar *d*-spacing (0.24, 0.16, 0.17, and 0.14 nm) well matched with XRD. Bi/MoS_2-doped SnO_2 in contrast with doped free sample elucidated supreme catalytic activity up to 99.9%. The significant inhibition zone was determined as 3.15 mm after doping at a high concentration. DFT calculation has completed the understanding of how MB molecules interacted with the Bi/MoS_2 doped SnO_2 QDs by exploring the electronic structure and absorption energy.

Data availability

Data will be available on demand.

Conflicts of interest

Manuscript is free from conflict of interest.

Acknowledgements

The authors are thankful to Higher Education Commission (HEC), Pakistan through NRPU-20-17615 (Dr Muhammad Ikram).

References

1 G. Zeng, M. Chen and Z. Zeng, Risks of neonicotinoid pesticides, *Science*, 2013, **340**(6139), 1403, DOI: 10.1126/science.340.6139.1403-a.

2 M. Razvigorova, T. Budinova, N. Petrov and V. Minkova, Purification of water by activated carbons from apricot stones, lignites and anthracite, *Water Res.*, 1998, **32**(7), 2135–2139, DOI: 10.1016/S0043-1354(97)00446-6.

3 J. Pal, M. K. Deb, D. K. Deshmukh and B. K. Sen, Microwave-assisted synthesis of platinum nanoparticles and their catalytic degradation of methyl violet in aqueous solution, *Appl. Nanosci.*, 2014, **4**(1), 61–65, DOI: 10.1007/s13204-012-0170-0.

4 X. Wang, M. Hong, F. Zhang, Z. Zhuang and Y. Yu, Recyclable nanoscale zero valent iron doped g-C_3N_4/MoS_2 for efficient photocatalysis of RhB and Cr(VI) driven by visible light, *ACS Sustainable Chem. Eng.*, 2016, **4**(7), 4055–4063, DOI: 10.1021/acssuschemeng.6b01024.

5 S. Pandey, J. Y. Do, J. Kim and M. Kang, Fast and highly efficient removal of dye from aqueous solution using natural locust bean gum based hydrogels as adsorbent, *Int. J. Biol. Macromol.*, 2020, **143**, 60–75, DOI: 10.1016/j.ijbiomac.2019.12.002.

6 S. Pandey and J. Ramontja, PTurning to Nanotechnology for Water Pollution Control: Applications of Nanocomposites, *Focus Sci.*, 2016, **2**(2), 1–10, DOI: 10.20286/focsci-020219.

7 L. Liu, B. Zhang, Y. Zhang, *et al.*, Simultaneous removal of cationic and anionic dyes from environmental water using montmorillonite-pillared graphene oxide, *J. Chem. Eng. Data*, 2015, **60**(5), 1270–1278, DOI: 10.1021/je5009312.

8 K. Sharma, G. Singh, M. Kumar and V. Bhalla, Silver nanoparticles: Facile synthesis and their catalytic application for the degradation of dyes, *RSC Adv.*, 2015, **5**(33), 25781–25788, DOI: 10.1039/c5ra02909k.

9 Y. Xian, F. Gao and B. Cai, Synthesis of platinum nanoparticle chains based on α-chymotrpsin fibrils, *Mater. Lett.*, 2013, **111**, 39–42, DOI: 10.1016/j.matlet.2013.08.051.

10 S. Eva Gnana Dhana Rani, A. Ganesh Kumar, S. Steplinpaulselvin, *et al.*, Survival assessment of simple food webs for dye wastewater after photocatalytic degradation using SnO_2/GO nanocomposites under sunlight irradiation, *Sci. Total Environ.*, 2020, **721**, DOI: 10.1016/j.scitotenv.2020.137805.

11 C. Nayral, E. Viala, V. Collière, *et al.*, Synthesis and use of a novel SnO_2 nanomaterial for gas sensing, *Appl. Surf. Sci.*, 2000, **164**(1–4), 219–226, DOI: 10.1016/S0169-4332(00)00340-8.

12 F. M. Courtel, E. A. Baranova, Y. Abu-Lebdeh and I. J. Davidson, In situ polyol-assisted synthesis of nano-SnO_2/carbon composite materials as anodes for lithium-ion batteries, *J. Power Sources*, 2010, **195**(8), 2355–2361, DOI: 10.1016/j.jpowsour.2009.10.086.

13 K. C. Pradel, Y. Ding, W. Wu, Y. Bando, N. Fukata and Z. L. Wang, Optoelectronic Properties of Solution Grown ZnO n-p or p-n Core-Shell Nanowire Arrays, *ACS Appl. Mater. Interfaces*, 2016, **8**(7), 4287–4291, DOI: 10.1021/acsami.5b11034.

14 K. L. Chopra, S. Major and D. K. Pandya, Transparent conductors-A status review, *Thin Solid Films*, 1983, **102**(1), 1–46, DOI: 10.1016/0040-6090(83)90256-0.

15 L. Cojocaru, C. Olivier, T. Toupance, E. Sellier and L. Hirsch, Size and shape fine-tuning of SnO_2 nanoparticles for highly efficient and stable dye-sensitized solar cells, *J. Mater. Chem. A*, 2013, **1**(44), 13789–13799, DOI: 10.1039/c3ta12279d.

16 Y. Zhang, Z. Hu, Y. Liang, *et al.*, Growth of 3D SnO_2 nanosheets on carbon cloth as a binder-free electrode for supercapacitors, *J. Mater. Chem. A*, 2015, **3**(29), 15057–15067, DOI: 10.1039/c5ta02479j.

17 Y. K. Mishra, G. Modi, V. Cretu, *et al.*, Direct Growth of Freestanding ZnO Tetrapod Networks for Multifunctional Applications in Photocatalysis, UV Photodetection, and Gas Sensing, *ACS Appl. Mater. Interfaces*, 2015, **7**(26), 14303–14316, DOI: 10.1021/acsami.5b02816.

18 S. Agarwal, I. Tyagi, V. K. Gupta, *et al.*, Iron doped SnO_2/Co_3O_4 nanocomposites synthesized by sol-gel and precipitation method for metronidazole antibiotic degradation, *Mater. Sci. Eng., C*, 2017, **70**, 178–183, DOI: 10.1016/j.msec.2016.08.062.

19 S. Pan, S. Wang, Y. Zhang, *et al.*, Surface Fe^{3+}-decorated pristine SnO_2 nanoparticles with enhanced ·OH radical generation performance, *Catal. Commun.*, 2012, **24**, 96–99, DOI: 10.1016/j.catcom.2012.03.034.

20 M. F. Abdel-Messih, M. A. Ahmed and A. S. El-Sayed, Photocatalytic decolorization of Rhodamine B dye using novel mesoporous SnO_2-TiO_2 nano mixed oxides prepared by sol-gel method, *J. Photochem. Photobiol., A*, 2013, **260**, 1–8, DOI: 10.1016/j.jphotochem.2013.03.011.

21 S. Bano, N. Ahmad, S. Sultana, S. Sabir and M. Z. Khan, Preparation and study of ternary polypyrrole-tin oxide-chitin nanocomposites and their potential applications in visible light photocatalysis and sensors, *J. Environ. Chem. Eng.*, 2019, **7**(2), DOI: 10.1016/j.jece.2019.103012.

22 P. O. Agboola and I. Shakir, Facile fabrication of SnO_2/MoS_2/rGO ternary composite for solar light-mediated photocatalysis for water remediation, *J. Mater. Res. Technol.*, 2022, **18**, 4303–4313, DOI: 10.1016/j.jmrt.2022.04.109.

23 S. Vadivel and G. Rajarajan, Effect of W doping on structural, optical and photocatalytic activity of SnO_2 nanostructure thin films, *J. Mater. Sci.: Mater. Electron.*, 2015, **26**(9), 7127–7133, DOI: 10.1007/s10854-015-3335-2.

24 S. B. Rawal, D. P. Ojha, Y. S. Choi and W. I. Lee, Coupling of W-Doped SnO_2 and TiO_2 for efficient visible-light photocatalysis, *Bull. Korean Chem. Soc.*, 2014, **35**(3), 913–918, DOI: 10.5012/bkcs.2014.35.3.913.

25 S. I. Siddiqui, F. Zohra and S. A. Chaudhry, Nigella sativa seed based nanohybrid composite-Fe_2O_3–SnO_2/BC: A novel material for enhanced adsorptive removal of methylene blue from water, *Environ. Res.*, 2019, **178**, 108667, DOI: 10.1016/j.envres.2019.108667.

26 Y. H. Tan, K. Yu, J. Z. Li, H. Fu and Z. Q. Zhu, MoS_2@ZnO nano-heterojunctions with enhanced photocatalysis and field emission properties, *J. Appl. Phys.*, 2014, **116**(6), DOI: 10.1063/1.4893020.

27 G. P. Awasthi, S. P. Adhikari, S. Ko, H. J. Kim, C. H. Park and C. S. Kim, Facile synthesis of ZnO flowers modified graphene like MoS_2 sheets for enhanced visible-light-driven photocatalytic activity and antibacterial properties, *J. Alloys Compd.*, 2016, **682**, 208–215, DOI: 10.1016/j.jallcom.2016.04.267.

28 K. H. Hu, X. G. Hu, Y. F. Xu and X. Z. Pan, The effect of morphology and size on the photocatalytic properties of MoS_2, *React. Kinet., Mech. Catal.*, 2010, **100**(1), 153–163, DOI: 10.1007/s11144-010-0173-3.

29 B. Pourabbas and B. Jamshidi, Preparation of MoS_2 nanoparticles by a modified hydrothermal method and the photo-catalytic activity of MoS_2/TiO_2 hybrids in photo-oxidation of phenol, *Chem. Eng. J.*, 2008, **138**(1–3), 55–62, DOI: 10.1016/j.cej.2007.05.028.

30 K. Chung Hui, W. Lun Ang and N. Soraya Sambudi, Nitrogen and bismuth-doped rice husk-derived carbon quantum dots for dye degradation and heavy metal removal, *J. Photochem. Photobiol., A*, 2021, **418**, 113411, DOI: 10.1016/j.jphotochem.2021.113411.

31 A. Raza, M. Ikram, M. Aqeel, *et al.*, Enhanced industrial dye degradation using Co doped in chemically exfoliated MoS_2 nanosheets, *Appl. Nanosci.*, 2020, **10**(5), 1535–1544, DOI: 10.1007/s13204-019-01239-3.

32 J. M. Small and H. Hintelmann, Methylene blue derivatization then LC-MS analysis for measurement of trace levels of sulfide in aquatic samples, *Anal. Bioanal. Chem.*, 2007, **387**(8), 2881–2886, DOI: 10.1007/s00216-007-1140-3.

33 C. G. Sinclair, Bergey's Manual of Determinative Bacteriology, *Am. J. Trop. Med. Hyg.*, 1939, **s1–s19**(6), 605–606, DOI: 10.4269/ajtmh.1939.s1-19.605.

34 A. W. Bauer, W. M. Kirby, J. C. Sherris and M. Turck, Antibiotic susceptibility testing by a standardized single disk method, *Am. J. Clin. Pathol.*, 1966, **45**(4), 493–496, DOI: 10.1093/ajcp/45.4_ts.493.

35 F. Adzitey, S. Yussif, R. Ayamga, *et al.*, Antimicrobial Susceptibility and Molecular Characterization of Escherichia coli Recovered from Milk and Related Samples, *Microorganisms*, 2022, **10**(7), 1335, DOI: 10.3390/microorganisms10071335.

36 NCCLS, *Performance Standards for Antimicrobial Susceptibility Testing*, Clin Lab Standars Inst - NCCLS, 2007, vol. 27, no. 1, pp. 1–182. doi:DOI: 10.3/JQUERY-UI.JS.

37 B. A. Iwalokun, A. Ogunledun, D. O. Ogbolu, S. B. Bamiro and J. Jimi-Omojola, In vitro antimicrobial properties of aqueous garlic extract against multidrug-resistant bacteria and Candida species from Nigeria, *J. Med. Food*, 2004, **7**(3), 327–333, DOI: 10.1089/jmf.2004.7.327.

38 A. Haider, M. I. Mustafa, M. Imran, *et al.*, Enhanced bactericidal action and dye degradation of spicy roots' extract-incorporated fine-tuned metal oxide nanoparticles, *Appl. Nanosci.*, 2019, **10**(4), 1095–1104, DOI: 10.1007/s13204-019-01188-x.

39 A. Haider, M. Ijaz, S. Ali, *et al.*, Green Synthesized Phytochemically (Zingiber officinale and Allium sativum) Reduced Nickel Oxide Nanoparticles Confirmed Bactericidal and Catalytic Potential, *Nanoscale Res. Lett.*, 2020, **15**(1), 50, DOI: 10.1186/s11671-020-3283-5.

40 M. Ikram, M. Imran, S. Hayat, *et al.*, MoS_2/cellulose-doped ZnO nanorods for catalytic, antibacterial and molecular docking studies, *Nanoscale Adv.*, 2022, **4**(1), 211–225, DOI: 10.1039/d1na00648g.

41 V. S. Kirankumar and S. Sumathi, Catalytic activity of bismuth doped zinc aluminate nanoparticles towards environmental remediation, *Mater. Res. Bull.*, 2017, **93**, 74–82, DOI: 10.1016/j.materresbull.2017.04.022.

42 S. Bagwasi, B. Tian, J. Zhang and M. Nasir, Synthesis, characterization and application of bismuth and boron Co-doped TiO_2: A visible light active photocatalyst, *Chem. Eng. J.*, 2013, **217**, 108–118, DOI: 10.1016/j.cej.2012.11.080.

43 E. Bartonickova, J. Cihlar and K. Castkova, Microwave-assisted synthesis of bismuth oxide, *Process. Appl. Ceram.*, 2007, **1**(1–2), 29–33, DOI: 10.2298/pac0702029b.

44 W. Raza, M. M. Haque, M. Muneer, T. Harada and M. Matsumura, Synthesis, characterization and photocatalytic performance of visible light induced

bismuth oxide nanoparticle, *J. Alloys Compd.*, 2015, **648**, 641–650, DOI: 10.1016/j.jallcom.2015.06.245.

45 R. Rahmi and F. Kurniawan, Synthesis of SnO_2 Nanoparticles by high potential electrolysis, *Bull. Chem. React. Eng. Catal.*, 2017, **12**(2), 281–286, DOI: 10.9767/bcrec.12.2.773.281-286.

46 S. Sivakumar and E. Manikandan, Novel Synthesis of Optical, Photoluminescence Properties and Supercapacitor Application on Zn^{2+} doping $Sn_{1-x}Zn_xO_2$ nanoparticles, *Int. J. Sci. Res. Phys. Appl. Sci.*, 2018, **6**(6), 1–13, DOI: 10.26438/ijsrpas/v6i6.113.

47 K. Skrabania, A. Miasnikova, A. M. Bivigou-Koumba, D. Zehm and A. Laschewsky, Examining the UV-vis absorption of RAFT chain transfer agents and their use for polymer analysis, *Polym. Chem.*, 2011, **2**(9), 2074–2083, DOI: 10.1039/c1py00173f.

48 M. Serhan, M. Sprowls, D. Jackemeyer, *et al.*, Total iron measurement in human serum with a smartphone, in *AIChE Annual Meeting, Conference Proceedings*, Novem, 2019, vol. 2019, pp. 1–7, doi:DOI: 10.1039/x0xx00000x.

49 Y. Zhou, X. Zhang, Q. Zhang, F. Dong, F. Wang and Z. Xiong, Role of graphene on the band structure and interfacial interaction of Bi_2WO_6/graphene composites with enhanced photocatalytic oxidation of NO, *J. Mater. Chem. A*, 2014, **2**(39), 16623–16631, DOI: 10.1039/c4ta03762f.

50 V. S. Kirankumar and S. Sumathi, Catalytic activity of bismuth doped zinc aluminate nanoparticles towards environmental remediation, *Mater. Res. Bull.*, 2017, **93**, 74–82, DOI: 10.1016/j.materresbull.2017.04.022.

51 F. C. Miguens, M. L. D. Oliveira, R. V. Marins and L. D. D. Lacerda, A new protocol to detect light elements in estuarine sediments by X-ray microanalysis (SEM/EDS), *J. Electron Microsc. (Tokyo)*, 2010, **59**(5), 437–446, DOI: 10.1093/jmicro/dfq013.

52 M. Naz, A. Rafiq, M. Ikram, *et al.*, Elimination of dyes by catalytic reduction in the absence of light: A review, *J. Mater. Sci.*, 2021, **56**(28), 15572–15608, DOI: 10.1007/s10853-021-06279-1.

53 A. Raza, J. Z. Hassan, M. Ikram, *et al.*, Molecular docking and DFT analyses of magnetic cobalt doped MoS_2 and BN nanocomposites for catalytic and antimicrobial explorations, *Surf. Interfaces*, 2021, **27**, 101571, DOI: 10.1016/j.surfin.2021.101571.

54 M. Ikram, R. Tabassum, U. Qumar, *et al.*, Promising performance of chemically exfoliated Zr-doped MoS_2 nanosheets for catalytic and antibacterial applications, *RSC Adv.*, 2020, **10**(35), 20559–20571, DOI: 10.1039/d0ra02458a.

55 M. Ikram, T. Inayat, A. Haider, *et al.*, Graphene Oxide-Doped MgO Nanostructures for Highly Efficient Dye Degradation and Bactericidal Action, *Nanoscale Res. Lett.*, 2021, **16**(1), 56, DOI: 10.1186/s11671-021-03516-z.

56 M. Ikram, S. Hayat, M. Imran, *et al.*, Novel Ag/cellulose-doped CeO_2 quantum dots for efficient dye degradation and bactericidal activity with molecular docking study, *Carbohydr. Polym.*, 2021, **269**, DOI: 10.1016/j.carbpol.2021.118346.

57 K. Anastasiadou, D. Axiotis and E. Gidarakos, Hydrothermal conversion of chrysotile asbestos using near supercritical conditions, *J. Hazard. Mater.*, 2010, **179**(1–3), 926–932, DOI: 10.1016/j.jhazmat.2010.03.094.

58 K. P. Singh, D. Mohan, S. Sinha, G. S. Tondon and D. Gosh, Color removal from wastewater using low-cost activated carbon derived from agricultural waste material, *Ind. Eng. Chem. Res.*, 2003, **42**(9), 1965–1976, DOI: 10.1021/ie020800d.

59 M. M. Sajid, H. Zhai, N. A. Shad, *et al.*, Construction of 1T-MoS_2 quantum dots-interspersed $(Bi_{1-x}Fe_x)VO_4$ heterostructures for electron transport and photocatalytic properties, *RSC Adv.*, 2021, **11**(22), 13105–13118, DOI: 10.1039/d1ra00807b.

60 S. N. Veedu, S. Jose, S. B. Narendranath, M. R. Prathapachandra Kurup and P. Periyat, Visible light-driven photocatalytic degradation of methylene blue dye over bismuth-doped cerium oxide mesoporous nanoparticles, *Environ. Sci. Pollut. Res.*, 2021, **28**(4), 4147–4155, DOI: 10.1007/s11356-020-10750-y.

61 L. Zhang, Y. Jiang, Y. Ding, M. Povey and D. York, Investigation into the antibacterial behaviour of suspensions of ZnO nanoparticles (ZnO nanofluids), *J. Nanopart. Res.*, 2007, **9**(3), 479–489, DOI: 10.1007/s11051-006-9150-1.

62 U. Qumar, M. Ikram, M. Imran, *et al.*, Synergistic effect of Bi-doped exfoliated MoS_2 nanosheets on their bactericidal and dye degradation potential, *Dalt Trans.*, 2020, **49**(16), 5362–5377, DOI: 10.1039/d0dt00924e.

63 C. Z. Chen and S. L. Cooper, Interactions between dendrimer biocides and bacterial membranes, *Biomaterials*, 2002, **23**(16), 3359–3368, DOI: 10.1016/S0142-9612(02)00036-4.

64 J. P. Perdew, K. Burke and M. Ernzerhof, Generalized gradient approximation made simple, *Phys. Rev. Lett.*, 1996, **77**(18), 3865–3868, DOI: 10.1103/PhysRevLett.77.3865.

65 S. Smidstrup, T. Markussen, P. Vancraeyveld, *et al.*, QuantumATK: An integrated platform of electronic and atomic-scale modelling tools, *J. Phys.: Condens. Matter*, 2020, **32**(1), 015901, DOI: 10.1088/1361-648X/ab4007.

66 M. J. van Setten, M. Giantomassi, E. Bousquet, *et al.*, The PSEUDODOJO: Training and grading a 85 element optimized norm-conserving pseudopotential table, *Comput. Phys. Commun.*, 2018, **226**, 39–54, DOI: 10.1016/j.cpc.2018.01.012.

67 S. Grimme, Semiempirical GGA-type density functional constructed with a long-range dispersion correction, *J. Comput. Chem.*, 2006, **27**(15), 1787–1799, DOI: 10.1002/jcc.20495.

68 J. Heyd, G. E. Scuseria and M. Ernzerhof, Hybrid functionals based on a screened Coulomb potential, *J. Chem. Phys.*, 2003, **118**(18), 8207–8215, DOI: 10.1063/1.1564060.

69 M. B. Kanoun, S. Goumri-Said, U. Schwingenschlögl and A. Manchon, Magnetism in Sc-doped ZnO with zinc vacancies: A hybrid density functional and GGA + U approaches, *Chem. Phys. Lett.*, 2012, **532**, 96–99, DOI: 10.1016/j.cplett.2012.02.055.

70 J. Haines and J. Léger, X-ray diffraction study of the phase transitions and structural evolution of tin dioxide at high

pressure:ffRelationships between structure types and implications for other rutile-type dioxides, *Phys. Rev. B: Condens. Matter Mater. Phys.*, 1997, **55**(17), 11144–11154, DOI: **10.1103/PhysRevB.55.11144**.

71 A. Raza, U. Qumar, A. Haider, *et al.*, Liquid-phase exfoliated MoS_2 nanosheets doped with: P-type transition metals: A comparative analysis of photocatalytic and antimicrobial potential combined with density functional theory, *Dalton Trans.*, 2021, **50**(19), 6598–6619, DOI: **10.1039/d1dt00236h**.

72 P. Tierney, T. J. Ennis, Á. Allen and J. Wright, The role of mid-band gap defect levels in persistent photoconductivity in RF sputtered SnO_2 thin films, *Thin Solid Films*, 2016, **603**, 50–55, DOI: **10.1016/j.tsf.2015.12.058**.

73 M. Behtash, P. H. Joo, S. Nazir and K. Yang, Electronic structures and formation energies of pentavalent-ion-doped SnO_2: First-principles hybrid functional calculations, *J. Appl. Phys.*, 2015, **117**(17), DOI: **10.1063/1.4919422**.

74 J. Hassan, S. Naz, A. Haider, *et al.*, h-BN nanosheets doped with transition metals for environmental remediation; a DFT approach and molecular docking analysis, *Mater. Sci. Eng., B*, 2021, **272**, DOI: **10.1016/j.mseb.2021.115365**.

75 S. Goumri-Said and M. B. Kanoun, Insight into the Effect of Anionic–Anionic Co-Doping on $BaTiO_3$ for Visible Light Photocatalytic Water Splitting: A First-Principles Hybrid Computational Study, *Catalysts*, 2022, **12**(12), DOI: **10.3390/catal12121672**.